

Analytic Design of Flat-Wire Inductors for High-Current and Compact DC-DC Converters

Sajjad Mohammadi
Electrical Engineering and Computer Science
MIT
Cambridge, USA
sajjadm@mit.edu

James L. Kirtley
Electrical Engineering and Computer Science
MIT
Cambridge, USA
kirtley@mit.edu

Alireza Namadmalan
Power Electronics & Magnetic Lab
Bourns Electronics Ireland (BEI).
Cork, Ireland
alireza.namadmalan@bourns.com

Abstract—This paper presents analytic study and design considerations of flat wire inductors with distributed gaps for high-power and compact DC-DC Converters. The focus is eddy-current loss components within the conductors due to fringing and leakage fluxes. A magnetic equivalent circuit (MEC) is proposed in which eddy currents are modeled by MMFs opposing the primary flux as well as frequency dependent reluctances, which finally leads to a frequency dependent inductance describing the behavior of the inductor at high frequencies. Three formulations for DC resistance depending on the required accuracy are developed. Calculations of the AC resistance based on vector potential obtained from FEM are provided. To provide an insight into the optimized design of such inductors, components of the magnetic flux and induced eddy currents along with sensitivity of the main inductor quantities such as DCR, ESR, loss components and inductance values to the design parameters are investigated. Finally, an inductor is prototyped and experimentally tested to verify the design.

Keywords—demagnetization, eddy-current coupler, finite element method, interior permanent magnet, wind generators.

I. INTRODUCTION

Recent advances in high-frequency and wide-band-gap semiconductors, such as GaN and SiC switches, have prioritized the miniaturization of power converters [1], where magnetic components, especially high-frequency inductors are usually the limiting components in terms of size and losses [2]-[5]. Typically, there are applications where current of high-power inductors include both high-frequency and low-frequency (or DC) components. These applications include DC-DC inductors, power factor correction (PFC) inductors, output filter inductors, and chokes [4]-[7]. The main challenge in these designs lies in selecting and designing the winding to manage both low and high-frequency conduction losses effectively [8].

Litz wire is a common solution to this challenge, yet its poor filling factor of about 50%, or sometimes less, limits its effectiveness for high power density applications. Compared to solid copper wires, litz wires leads to bulkier inductors with higher direct current resistance (DCR), negatively impacting low-frequency or DC performance. However, poorly designed solid wires can lead to increased equivalent series resistance (ESR) at high frequencies [8]. Various solutions using solid copper wires aim to optimize the balance between DCR and ESR at high frequencies. For example, a design using single-

layer winding of round wires can reduce ESR for high-frequency applications [9]. Although it works well for toroidal shapes, it presents high ESR for multi-layer designs [10].

Solid wires with spiral shape, although promising, are mainly suitable for PCB inductors [2]. Solid flat wires, although provide a better thermal conductivity and DCR, require careful design optimization [7]. Among solid wire options, flat spiral and helix shapes offer superior performance and offer more practical manufacturing on printed circuit boards (PCBs), helping to reduce the size of the magnetic components. Spiral shapes, though effective, have proximity effect issues and are more suitable for high-frequency planar transformers [2].

Beside superior benefits for solid flat wire inductors, still they require further research in terms of accurate modelling [7], and [10]. To do design optimization of such inductors, e.g. using heuristic methods presented in [12], accurate models are needed to derive analytical equations for AC and DC losses in the solid flat wire coils. The model should consider the frequency-dependent effects of eddy-currents, reluctance paths and fringing effect of the core's gaps, which has not been proposed for such inductors. As an example, [13]-[14] has presented such a model for eddy currents in the lamination and magnets of an actuator, where eddy current impacts are represented as frequency-dependent reluctance and inductance.

The main contribution of this paper is presenting an analytic study and design considerations of high-power inductors with helical flat wires and distributed gaps with a focus on eddy-current effects in the coil. A magnetic equivalent circuit (MEC) including magneto-motive forces or frequency-dependent reluctances is offered which explain the inductance reduction at higher frequencies. Equations for DC and AC resistances for three cases are developed. FEM is employed in the analyses. Flux and eddy current components as well as the impact of design parameters on the performance indices of the inductor are investigated. Finally, an inductor with PQ 40/40 ferrite core is prototyped and tested to experimentally verify the design.

II. INDUCTOR TOPOLOGY

Fig. 1 shows an inductor including a PQ 40/40 core with a distributed gap and a flat-wire coil. As the fringing fluxes almost take a circular path with an effective radius of the gap length, as

illustrated in Fig. 2, distributing a large gap into multiple small gaps leads to less penetration of the fringing flux into the window, resulting in less eddy current loss.

III. COUPLED MAGNETIC-ELECTRIC CIRCUIT

Figs. 3 (a)-(b) show flux lines, flux density and field intensity within the inductor for a DC current of 5 A with no eddy-current effect. It is a two-dimensional FEM with a symmetry along ϕ axis. We have flux fringing at the gaps and a leakage through the window. Field intensity distribution shows that most of the stored energy is mainly within the air-gap, and then the fringing regions.

Accordingly, magnetic equivalent circuit shown in Fig. 4(a) can be developed in which R_g , R_{ci} , R_f , and R_{lw} are gap reluctance, i^{th} core reluctance, fringing reluctance and window leakage reluctance. As shown in Fig. 4(b), eddy currents induced in the conductors by fringing or window leakage fluxes can be modeled by magneto-motive forces F_{ef} and F_{ew} , respectively, which generate fluxes ϕ_{ef} and ϕ_{ew} in the opposite direction of the original flux generated by the coil in the fringing region and the window, respectively. As represented in Fig. 4(c), it can be shown that these MMFs can be modeled by frequency dependent reluctances $R_{ef}(j\omega)$ and $R_{ew}(j\omega)$ in series with the primary zero-frequency reluctance. These frequency-dependent reluctances go up at higher frequencies which explains why inductance goes down by a reduction in the total flux linked by the coil at higher frequencies [13]-[14].

$$\varphi(j\omega) = \frac{Ni_L}{R_t(j\omega)} = \frac{Ni_L}{R_0 + \underbrace{R_0 Q(j\omega)}_{R_e(j\omega)}} = \frac{Ni_L}{R_0(1+Q(j\omega))} \quad (1)$$

where R_t is the total reluctance, R_0 is the total reluctance at zero frequency and R_e is the total reluctance added by eddy currents which is zero at zero frequency with Q as an auxiliary term:

$$\omega \rightarrow 0 \Rightarrow Q(j\omega) \rightarrow 0; R_e(j\omega) \rightarrow 0; R_t(j\omega) \rightarrow R_0; \varphi(j\omega) \rightarrow \phi_0 \quad (2)$$

where ϕ_0 is the primary flux at zero frequency:

$$\phi_0 = \frac{Ni_L}{R_0} \quad (3)$$

The coupled electric-magnetic circuit for both zero-frequency case and the frequency-dependent case are shown in Fig. 5. The governing equations can be expressed as:

$$\begin{cases} V_L = R_L I_L + j\omega N \varphi \\ NI_L = R_i \varphi \end{cases} \Rightarrow \begin{bmatrix} R_L & j\omega N \\ -N & R_i \end{bmatrix} \begin{bmatrix} I_L \\ \varphi \end{bmatrix} = \begin{bmatrix} V_L \\ 0 \end{bmatrix} \quad (4)$$

There is a codependency between electrical and magnetic circuits. From the magnetic circuit, flux is returned to the electrical circuit, and from the electrical circuit, the current is returned to the magnetic circuit. By solving the above system of equation, the terminal impedance can be obtained as:

$$Z(j\omega) = \frac{V_L}{I_L} = R_L + j\omega L(j\omega); L(j\omega) = \frac{N^2}{R_t(j\omega)} = \frac{L_0}{1+Q(j\omega)} \quad (5)$$

It can be seen that the inductance $L(j\omega)$ is L_0 at zero frequency, and at higher frequencies, as Q and subsequently the reluctance goes up, the inductance goes down.

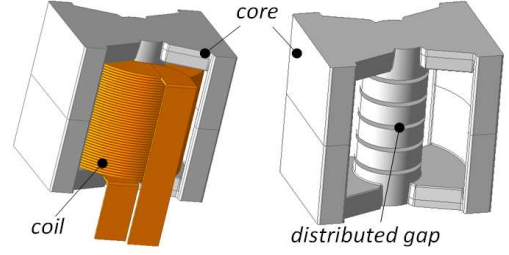


Fig. 1. Topology (top) and exploded view (bottom) of the proposed coupler.

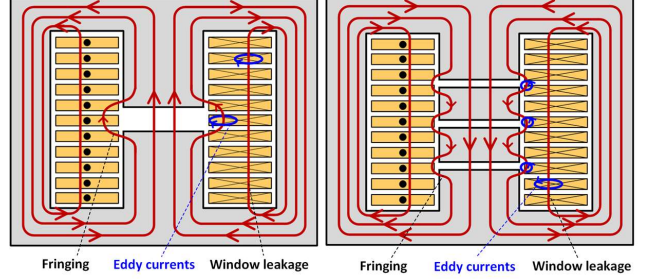


Fig. 2. Flux paths for inductors with single and distributed gaps.

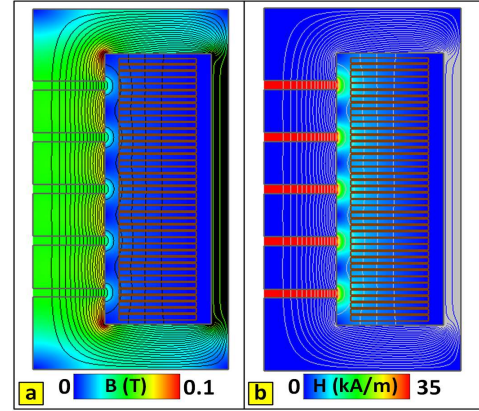


Fig. 3. Flux lines, flux density and field intensity with the core and window.

IV. DC RESISTANCE AND LOSS

Three models for calculating DCR are represented here that can be employed depending on the inductor topology and the required accuracy.

A. Coil with Helical Shape

Fig. 6 shows the geometry of the coil in which R_w , D_w , t_w , h_w , s , N are inner radius of the coil, radial length of the coil, thickness or z -height of the flat wire, total height of the coil, distance between turns, and number of turns, respectively. Moreover, D_{righ} and D_{left} are clearance between coil and core, shown in Fig. 6. A differential area of $dA = t_w dr$ for a differential radius of dr is employed in the integration. Using the length of helix $l(r)$ with radius r , N , and a total height of $h_w = Nt_w + (N-1)s$, the conductance is obtained as:

$$G_{DC} = \frac{1}{R_{DC}} = \int_{r=R_w}^{r=R_w+D_w} \frac{\sigma t_w dr}{l(r)} \quad (6)$$

where the total length of the coil with N turns is as follows:

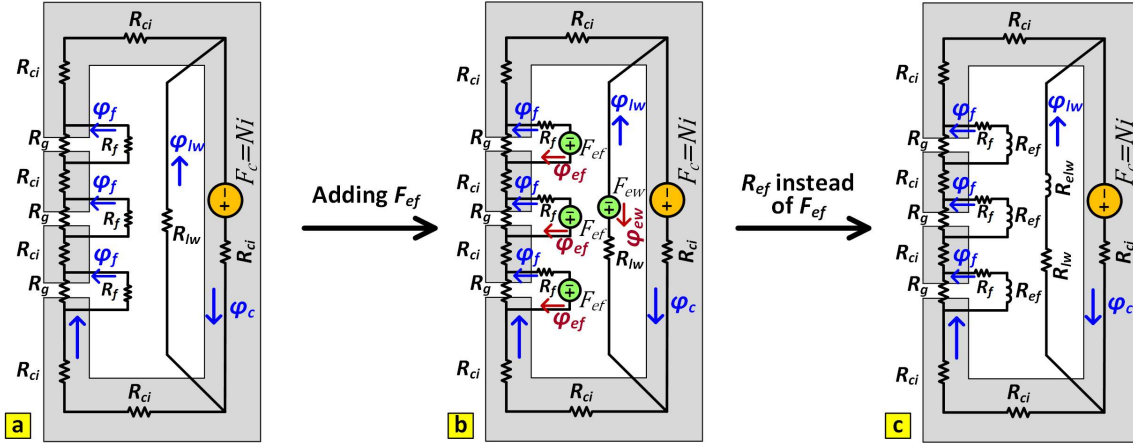


Fig. 4. MEC development: (a) eddy-currents ignored, (b) MMFs F_e representing eddy-currents an opposing flux, and (c) frequency-dependent reluctances R_e .

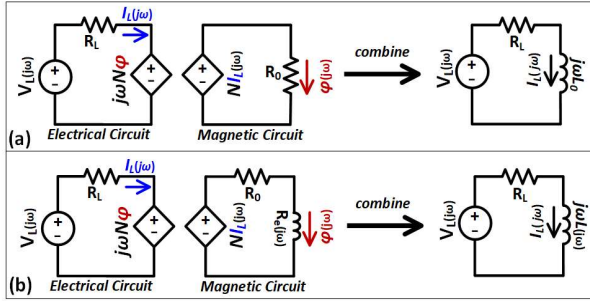


Fig. 5. Coupled electric-magnetic circuit: (a) low frequency case with no frequency dependency, and (b) frequency dependency due to eddy currents.

$$l(r) = 2\pi N \sqrt{r^2 + \left(\frac{h_w}{2\pi N}\right)^2} \quad (7)$$

Finally, DCR is obtained as:

$$R_{DC} = 2\pi N / \left\{ \sigma t_w \ln \left[\frac{r_w + D_w + \sqrt{(r_w + D_w)^2 + \left(\frac{h_w}{2\pi N}\right)^2}}{r_w + \sqrt{r_w^2 + \left(\frac{h_w}{2\pi N}\right)^2}} \right] \right\} \quad (8)$$

This is the general and the most accurate relationship for calculation of the DCR of this type of coil which is particularly useful for small number of turns where $h_w/2\pi N$ is not small compared to $r_w + D_w$.

B. Planar Circular Approximation

For large number of turns, coil length can be approximated by discrete circular turns as follows. It can also be obtained from approximation of the previous equation if $h_w/2\pi N$ is small enough and negligible. The conductance can be derived as:

$$G_{DC} = \frac{1}{R_{DC}} = \int_{r=r_w}^{r=r_w+D_w} \frac{\sigma t_w dr}{l(r)} \quad (9)$$

where the total length of the coil with N turns is as follows:

$$l(r) = 2\pi N r \quad (10)$$

Finally, DCR is obtained as:

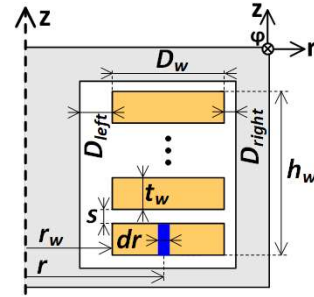


Fig. 6. Coil dimensions.

$$R_{DC} = 2\pi N / \left\{ \sigma t_w \ln \left(\frac{r_w + D_w}{r_w} \right) \right\} \quad (11)$$

C. Average Radius Approximation

An initial estimation of DCR can be obtained by considering an average radius $R_{av} = r_w + D_w/2$ as follows:

$$G_{DC} = \frac{1}{R_{DC}} = \int_{r=r_w}^{r=r_w+D_w} \frac{\sigma t_w dr}{l(r)} \quad (12)$$

where the total length of the coil with N turns is as follows:

$$l(r) = 2\pi N R_{av} \quad (13)$$

Finally, DCR is obtained as:

$$R_{DC} = \frac{2\pi N R_{av}}{\sigma t_w D_w} \quad (14)$$

V. AC RESISTANCE AND CONDUCTION LOSSES

This section is devoted to the calculations of AC resistance of the inductor at high frequencies. According to Gauss's law $\nabla \cdot B = 0$, a magnetic vector potential A can be defined as $B = \nabla \times A$. Employing the identity $\nabla \times \nabla \times A = \nabla(\nabla \cdot A) - \nabla^2 A$ and Coulomb's gauge condition $\nabla \cdot A = 0$ in Ampere's law yields:

$$\nabla \times H = J \xrightarrow{H=B/\mu_0} \nabla \times \left(\frac{\nabla \times A}{\mu_0} \right) = J \rightarrow \nabla^2 A = -\mu_0 J \quad (15)$$

In the two-dimensional domain with symmetry in the ϕ direction, the vector potential A_ϕ and the currents J_ϕ are in the

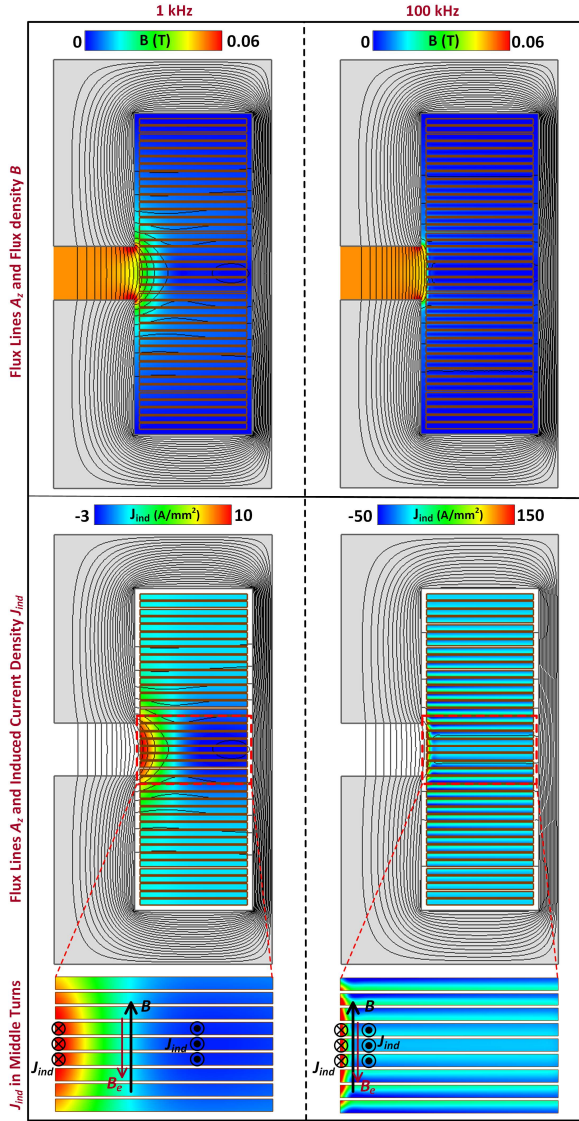


Fig. 7. Flux lines, flux density, and induced eddy currents in the conductors at frequencies of 1 kHz and 100 kHz for inductor with single large gap.

ϕ direction, while magnetic fields B and H are in the rz -plane. We have:

$$\nabla^2 A_\phi(r, z, t) = -\mu_0 J_\phi(r, z, t) \quad (16)$$

It is a 2-D problem with ϕ -directed current J_ϕ that can be decomposed into the source $J_s(t)$ due to inductor terminal current, and also induced eddy-current density J_{eddy} . As follows:

$$J_\phi(r, z, t) = J_s(t) + J_{eddy}(r, z, t) \quad (17)$$

The inductor terminal current I_L can be obtained by integrating J_s which is uniformly distributed over a conductor area as follows:

$$I_L(t) = \iint_{A_w} J_s(t) dr dz = t_w D_w J_s(t) \quad (18)$$

Using Faraday's law and Ohm's law $J_\phi = \sigma E_\phi$, induced eddy current density can be obtained in terms of A_ϕ as follows:

$$\nabla \times E_\phi(r, z, t) = -\frac{\partial B_{rz}(r, z, t)}{\partial t} \xrightarrow{B=\nabla \times A} E_\phi(r, z, t) = -\frac{\partial A_\phi(r, z, t)}{\partial t}$$

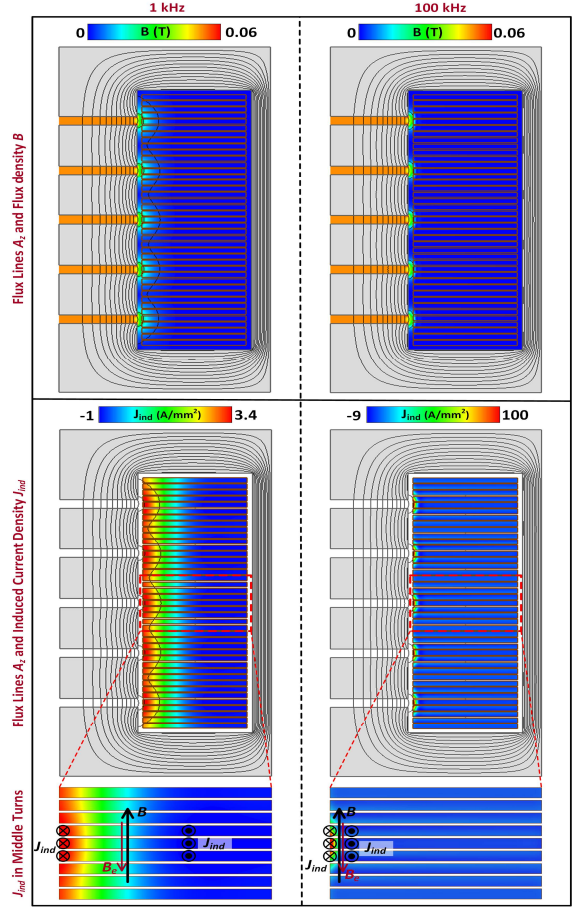


Fig. 8. Flux lines, flux density, and induced eddy currents in the conductors at frequencies of 1 kHz and 100 kHz for distributed gap inductor if conductors are close to the gap (small D_{left}).

Then, (19)

$$J_{eddy}(r, z, t) = -\sigma \frac{\partial A_\phi(r, z, t)}{\partial t} \quad (20)$$

In the phasor domain, we obtain:

$$J_{eddy}(r, z, j\omega) = -j\omega\sigma A_\phi(r, z, j\omega) \quad (21)$$

The AC resistance R_{ac} is the effective resistance seen at terminals that can be obtained from dissipated power as:

$$P = R_{ac} I_L^2 = \iiint_{volume} \frac{|J_\phi(r, \phi, z)|^2}{\sigma} dr d\phi dz = \frac{2\pi}{\sigma} \iint_{Area} |J_\phi(r, z)|^2 dr dz \quad (22)$$

Substituting J_ϕ in terms of its components leads to:

$$R_{ac} = \frac{2\pi}{\sigma} \frac{\iint_{Area} |J_s + J_{eddy}(r, z)|^2 dr dz}{I_L^2} \quad (23)$$

VI. EDDY-CURRENT DESOMPOSITION AND DESIGN CONSIDERATIONS

In this section, eddy current components induced in the coil due to leakage or fringing fluxes are analyzed to provide a deeper insight into the design of the inductor with minimized

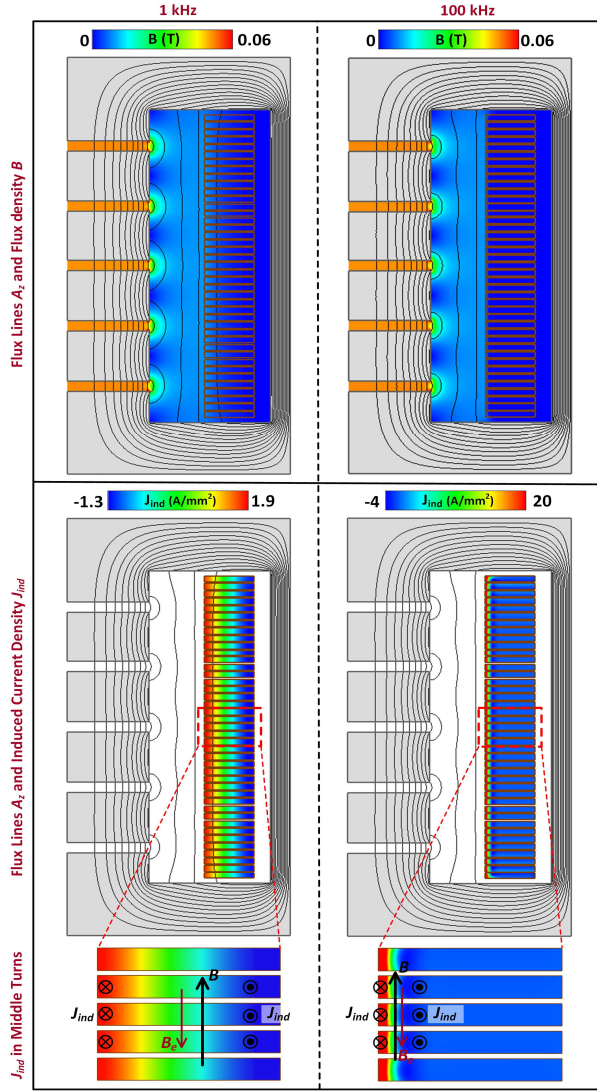


Fig. 9. Flux lines, flux density, and induced eddy currents in the conductors at frequencies of 1 kHz and 100 kHz for distributed gap inductor if conductors are away from the gap (large D_{gap}).

conductive loss. Figs. 7-10 provide flux lines, flux density and induced eddy currents at a low frequency of 1 kHz and a high frequency of 100 kHz under various scenarios.

Also, Fig. 11 shows the impact of design parameters on inductors quantities including DC and AC resistances, loss components, and inductance.

As shown in Figs. 7-8, the fringing fluxes at the gap of an inductor with a single large gap flows into a large volume of conductors, while the fringing fluxes in the inductor with distributed gap are limited to smaller areas, leading to smaller eddy current losses in the conductor. It should be noted that, in order to show the closed loops of the induced eddy currents in $+\phi$ and $-\phi$ directions, the current density plots illustrate only the induced eddy currents J_{eddy} , not the total current J_{ϕ} . It can be seen that the vertical field B due to gap fringing fluxes or the window leakage flux which are in the z direction induce circulating eddy currents in the $r-\phi$ plane.

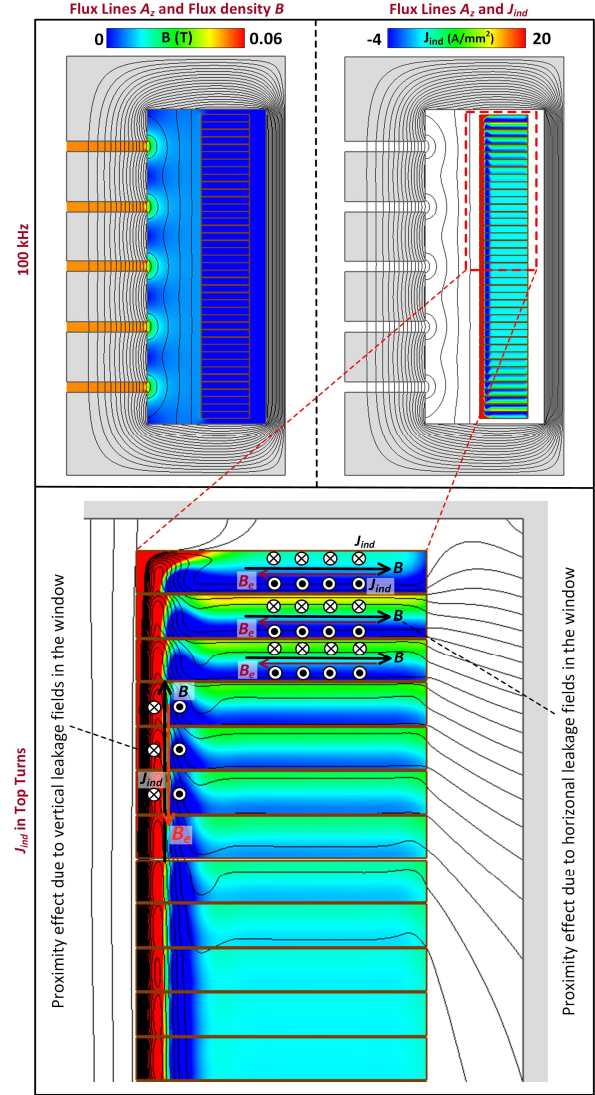


Fig. 10. Flux lines, flux density, and induced eddy currents in the conductors at frequencies of 1 kHz and 100 kHz for distributed gap inductor if conductors are very close to each other (small s).

As expected, the reaction fields B_e generated by induced eddy currents are in the opposite direction of the initial field B which explains how eddy currents reduce the flux linked by the coil λ and thus the inductance $L = \lambda/i$ at higher frequencies. It can also be observed that, at 100 kHz, induced currents penetrate less into the depth of the conductor and mostly concentrate at the inner radius of the coil with a higher magnitude.

As shown in Fig. 9, there is a leakage flux within the window. The larger the total air-gap or the higher the core saturation, the larger the window leakage. In other words, if the reluctance of the main flux path within the core goes up, a larger portion of flux tends to flow into the window. These vertical fluxes cause eddy currents circulating in the $r-\phi$ plane which will be limited to the inner radius of conductors at higher frequencies, and also the window leakage flux will be confined to the inner section of the window while they also penetrate into the coil area at the lower frequencies.

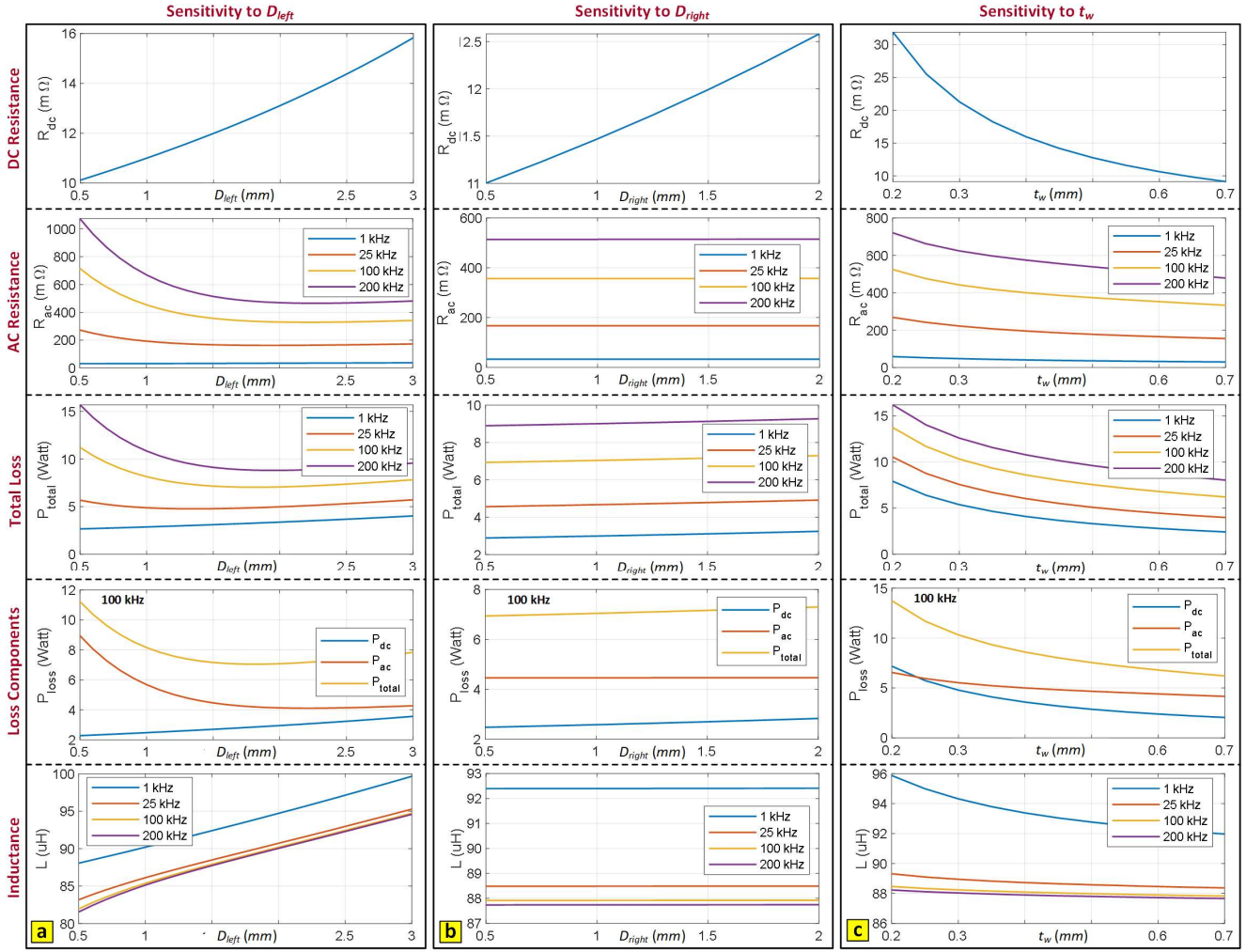


Fig. 11. Sensitivity of DC resistance, AC resistance, loss components, and inductance to design variables.

Fig. 10 represents finite element analysis for a case with small vertical distance s between the turns to study proximity between coil turns. Due to the horizontal leakage fluxes in the window, eddy-currents are induced in the z - ϕ plane.

It is seen in Fig. 11(a) that, as the coil distance from the gaps D_{left} is increased, the induced eddy currents are decreased, and therefore, AC resistance and AC losses go down, while DC resistance and DC loss go up due to smaller coil cross section. It shows an optimal point to achieve the minimum total loss. As leakage flux within the window is rejected by eddy currents in the conductors, this leakage flux exists only within the area between the inner radius of the coil and the core. Therefore, the inductance linearly goes up with D_{left} as this area goes up linearly.

As shown in Fig. 11(b), the DC resistance and DC loss go up with increasing the distance between the outer radius of the coil and the core D_{right} . However, as the eddy currents are mostly induced on the left side of the coil near the gaps, the AC resistance and AC loss are not affected by increasing the coil distance from the right side. Additionally, the inductance is not affected by D_{right} as fringing and window leakage fluxes are rejected by the inner radius of the coil. Fig. 11(c) suggests that,

by increasing the coil thickness t_w , the DC resistance and loss goes down, and also AC resistance and AC loss go down as the skin effect goes down. However, inductance goes down due to flux rejection by the induced eddy currents.

VII. PROTOTYPE AND EXPERIMENTAL RESULTS

As shown in Fig. 12(a), a flat wire inductor with five distributed gaps of 1 mm each using a PQ 40/40 ferrite core is prototyped and tested, as shown in Fig. 12 (b), to verify the analytical modeling. The prototype has $87 \mu\text{H} \pm 10\%$ with 30% drop at 34 A under 100°C . The specifications are $N = 41$, $t_w \approx 0.58$ mm, $D_w = 8$ mm, $s \approx 0.13$ mm and $r_w = 9.0$ mm, based on PQ 40/40 core with N95 material.

Inductance and AC resistance values versus frequency are shown in Fig. 13 (a) and (b) using WYNE KERR 6500B impedance analyzer. As seen, at operating frequency of 100 kHz, L is measured about $82.8 \mu\text{H}$ with 5.8% discrepancy from $L=87.9 \mu\text{H}$ obtained by FEM. Furthermore, ac-resistance is measured about 500 m Ω , which here is combination of winding's ESR and the ESR reflected from the PQ40/40 core. To exclude the reflected resistance from the core, first ESR of a reference inductor made by 170x0.05 mm litz wire, with $N = 41$

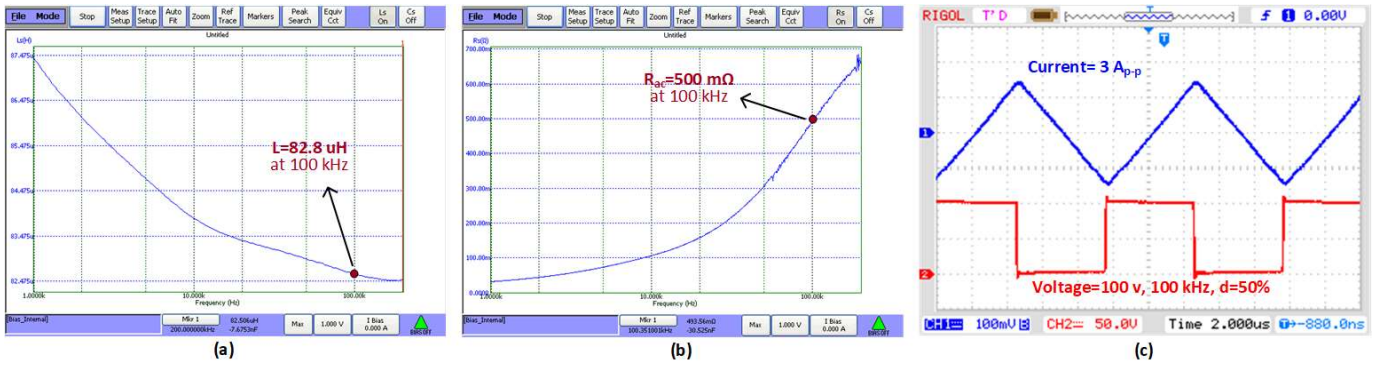


Fig. 13. Measurements of (a) inductance versus frequency, (b) AC resistance versus frequency and (c) voltage and current waveforms at 100 kHz with duty cycle of =50 %.

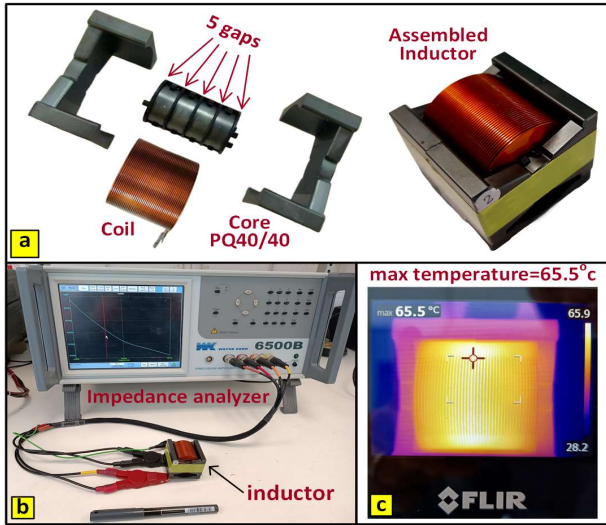


Fig. 12. Experiment: (a) prototype, (b) measurement setup, and (c) thermal camera.

and the same core is measured. Regarding FEM simulations, AC and DC resistances of the litz wire are very close to each other for 100 kHz, less than 10% changes. Hence the measured ESR of the reference inductor is approximately equal to its DCR plus the extra ESR reflected from the core [10].

Using WYNE KERR 6500B impedance analyser and for 100 kHz, the ESR reflected from core is estimated about 75 mΩ, by excluding DCR of the litz wire from the total ESR measured by the impedance analyser.

Hence, for the flat wire prototype, ESR of the winding is estimated about 425 mΩ with 19 % deviation from 357mΩ of FEM (discrepancy is due to the 3D impacts, especially large leakage fluxes in the two conductor regions without a surrounding core which causes more eddy currents losses). The DCR of the flat wire inductor is measured 12.4 mΩ, with 3.3% deviation from 12 mΩ obtained by equations (1) and (2).

Furthermore, the inductor has been utilized in a synchronous buck converter using LMG342XEVM-04 GaN daughter card from Texas Instruments. The converter's topology is selected as a buck converter, shown in Fig. 14. The buck converter has been tested from 1 kHz to 200 kHz with input voltage V_{in} from 10 V up to 200 V. The load is selected a variable resistive load capable

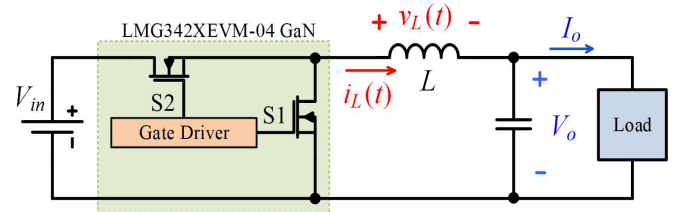


Fig. 14. Test circuit: buck converter.

of handling 0 up to 20 A. Fig. 13 (c) shows the inductor's current ripple at switching frequency of 100 kHz, 50% duty cycle and input voltage of 100 V. In this condition, the current probe is connected through AC-coupling condition, showing only the ac ripple current.

Values reported for the ac inductance, included in Fig. 11, have been verified by accurate measuring the peak-to-peak ripple current, I_{pp} , of the inductor and knowing V_{in} and switching frequency, f_s , under duty cycle of 50 %:

$$L = \frac{V_{in}}{2I_{pp}f_s} \quad (24)$$

Comparing the values derived experimental results and the values presented in Fig. 11, the maximum deviation was reported about 7.5 % for 1, 25, 100 and 200 kHz operating conditions. To illustrate the thermal performance, steady-state temperature of inductor with the same switching pattern and a DC current of 15 A is shown Fig. 12(c). With a temperature rise of 40 °C from ambient temperature of 25 °C, the inductor temperature of 65 °C is still well below 100 °C which is satisfactory.

VIII. CONCLUSION

Analytic study and design considerations for flat wire inductors are presented. Magnetic equivalent circuits including frequency-dependent reluctances and inductance are introduced. Three formulations for DCR are derived which can be used depending on the coil topology and the required accuracy. Calculations for ESR and AC losses are presented. Effectiveness of distributed gaps in terms of reduced fringing flux and thus eddy current losses is shown. Eddy current components are scrutinized. Sensitivity of inductor quantities such as DCR, ESR, loss components and inductance to design parameters are studied. The optimum design and the balance

between *DCR* and *ESR* are discussed. Finally, an inductor is prototyped, where the experimental results are on par with FEM and show the satisfactory performance of the design.

REFERENCES

- [1] F. C. Lee, S. Wang and Q. Li, "Next Generation of Power Supplies—Design for Manufacturability," *IEEE Journal of Emerging and Selected Topics in Power Electronics*, vol. 9, no. 6, pp. 6462-6475, Dec. 2021.
- [2] M. Sato, Y. Hattori, M. Ueda, Y. Bu and T. Mizuno, "Improved Performance of a Flat-Wire Coil with Magnetic Composite Material for Wireless Power Transfer," *IEEE Magnetics Letters*, vol. 12, pp. 1-5, 2021.
- [3] Jiankun Hu and C. R. Sullivan, "AC resistance of planar power inductors and the quasi-distributed gap technique," *IEEE Transactions on Power Electronics*, vol. 16, no. 4, pp. 558-567, July 2001.
- [4] R. Jez, "Influence of the Distributed Air Gap on the Parameters of an Industrial Inductor," *IEEE Transactions on Magnetics*, vol. 53, no. 11, pp. 1-5, Nov. 2017.
- [5] C. Kjeldsen, C. Østergaard, M. Nymand and R. Ramachandran, "Procedure to compare different design methods for implementation-ready high power inductors," *2019 IEEE 13th International Conference on Compatibility, Power Electronics and Power Engineering (CPE-POWERENG)*, Sonderborg, Denmark, 2019, pp. 1-6.
- [6] Y. Zhang, X. Guo, G. Wang and Q. Xiao, "A Novel Power Inductor and Its Application for Compact, Large Current DC-DC Converters," *2021 IEEE Applied Power Electronics Conference and Exposition (APEC)*, Phoenix, AZ, USA, 2021, pp. 2865-2869.
- [7] L. Wang, W. Liu, D. Malcom and Y. -F. Liu, "An Integrated Power Module Based on the Power-System-In-Inductor Structure," *IEEE Transactions on Power Electronics*, vol. 33, no. 9, pp. 7904-7915, Sept. 2018.
- [8] R. P. Wojda and M. K. Kazimierczuk, "Winding Resistance and Power Loss of Inductors with Litz and Solid-Round Wires," *IEEE Transactions on Industry Applications*, vol. 54, no. 4, pp. 3548-3557, July-Aug. 2018.
- [9] D. K. Saini, A. Ayachit, A. Reatti and M. K. Kazimierczuk, "Analysis and Design of Choke Inductors for Switched-Mode Power Inverters," *IEEE Transactions on Industrial Electronics*, vol. 65, no. 3, pp. 2234-2244, March 2018.
- [10] A. Namadmalan, "Modeling of High Power Inductors Based on Solid Flat Wires for Compact DC-DC Converters," *2024 IEEE Kansas Power and Energy Conference (KPEC)*, Manhattan, KS, USA, 2024, pp. 1-5.
- [11] R. Rajamony, S. Wang, R. Navaratne and W. Ming, "Multi-Objective Design of Single-Phase Differential Buck Inverters with Active Power Decoupling," *IEEE Open Journal of Power Electronics*, vol. 3, pp. 105-114, 2022.
- [12] A. Namadmalan, B. Jaafari, A. Iqbal and M. Al-Hitmi, "Design Optimization of Inductive Power Transfer Systems Considering Bifurcation and Equivalent AC Resistance for Spiral Coils," *IEEE Access*, vol. 8, pp. 141584-141593, 2020.
- [13] S. Mohammadi, W. R. Benner, J. L. Kirtley, and J. H. Lang, "An Actuator with Magnetic Restoration, Part I: Electromechanical Model and Identification," *IEEE Transactions on Energy Conversion*, 2024, doi:10.1109/TEC.2024.3387390.
- [14] S. Mohammadi, "Modeling, Design, Identification, Drive, and Control of a Rotary Actuator with Magnetic Restoration," Ph.D dissertation, Department of Electrical Engineering and Computer Science., Massachusetts Institute of Technology, 2022.